Mechanisms of picosecond laser-induced damage from interaction with model contamination particles on a high reflector

Kyle R. P. Kafka,* Brittany N. Hoffman, Hu Huang, and Stavros G. Demos
University of Rochester, Laboratory for Laser Energetics, Rochester,
New York, United States

Abstract. The interactions of microparticles of different materials located on the surface of a multilayer dielectric mirror with intense 1053-nm laser pulses of varying fluence and duration (10 and 0.6 ps) are investigated. The particles caused localized intensification of the electric field, which becomes the dominant mechanism for the onset of damage and secondary contamination of the mirror at fluences far below the pristine (without particles) laser-induced-damage threshold of the mirror. Several interaction mechanisms leading to material modification and damage are identified, including the localized field intensification by multibeam interference and particle-induced microlensing, plasma-induced scalding, and secondary contamination via nanoparticle generation and particle melting. The resulting morphologies were observed to be vulnerable to damage growth and additional damage initiation when irradiated by subsequent pulses. © *2020 Society of Photo-Optical Instrumentation Engineers (SPIE)* [DOI: 10.1117/1.OE.60.3.031009]

Keywords: laser damage; contamination; microparticles; field enhancement.

Paper 20201090SS received Sep. 15, 2020; accepted for publication Dec. 11, 2020; published online Dec. 30, 2020.

1 Introduction

High-energy laser pulses generated by large-aperture laser systems produce, when focused on small areas on materials, extreme conditions in a laboratory environment, such as temperatures and pressures that exist in the cores of stars and giant planets or electric fields that produce relativistic and ultrarelativistic interactions. The potential benefits from advancing fundamental understanding of materials under extreme conditions have facilitated a great interest, and a number of such laser systems have been completed during the past 10 years or are under construction. There are three general classes of such lasers. The first class uses nanosecond pulses that are temporally tailored to study the materials under high pressures and temperatures including nuclear fusion conditions [the National Ignition Facility (NIF), Laser Mégajoule (LMJ), SG-III, and OMEGA].[1–4] The second class uses femtosecond pulses and aims at achieving high peak intensities on a target to study a plurality of effects including quantum electrodynamics and temporally resolve the electron dynamics in materials (extreme light infrastructure, Shanghai Super-intense Ultrafast Laser Facility, and Advanced Photonics Research Institute).[5–7] The third class of lasers operates in the 1-ps regime and is typically used not only for the generation of diagnostic beams complementing higher-energy nanosecond-class laser systems but also for independent research such as for nuclear fusion and high-peak-intensity-related research [PETAL, OMEGA EP, NIF ARC, LFEX (Laser for Fast Ignition Experiment)].[8–11]

Due to the large aperture of their optical elements, the cost for their replacement after they have sustained laser-induced damage is significant. Consequently, the output power of these systems is largely limited by the fluences that the optical elements can withstand without unsustainable damage issues to maintain the operational cost sufficiently low. Although laser-induced damage is an issue affecting all high-power lasers, including tabletop systems, large-aperture

---

*Address all correspondence to Kyle R. P. Kafka, kkaf@lle.rochester.edu systems can still operate within specifications even after sustaining some damage on the optics. This necessitates a multifaceted management of the laser-damage problem, where part of the focus shifts from the initial damage performance of the optical components to maintaining this performance over long time durations by (a) preventing the generation of new damage sites and (b) arresting the growth of the existing damage sites.

Considering this objective of long-term performance, the important role of contamination of the optical elements has been recognized for nanosecond-class lasers.[12–17] Specifically, contamination particles can become the source of damage initiation via a number of mechanisms, depending on the contamination material (such as metal or dielectric) and optical substrate (such as reflective or transmissive) properties. The contamination of the optical elements not only can occur during installation but also can originate from the operational environment and the long-term damage performance of the optics. Work has demonstrated that laser damage with nanosecond pulses can cause particle ejection from the affected optics that can transport onto adjacent optics and become the source of damage initiation.[18] It has also been shown that "ghost" beams from the secondary reflections that may be focused on the side walls can cause particle ejection and contamination of the system optics.[19]

The potential for analogous processes occurring in short-pulse laser systems has received much less attention. It has been shown that organic contamination in the LFEX laser pulse compressor caused the damage threshold to decline to 1/2 or 1/3 of the original value.[20] A degradation with time of the damage performance in the OMEGA EP compression gratings[21] has also been reported, although the origin of this problem remains unresolved. We recently demonstrated, using model contamination particles (including metal, glass, and plastic spherical particles) located on the surface of a multilayer dielectric mirror, that exposure to 0.6- and 10-ps pulses at 1053 nm can introduce damage at fluences that are significantly lower than that of the pristine surface and can also introduce secondary contamination.[22]

Motivated by these results, we performed a more-detailed survey of the OMEGA EP chamber and found a plurality of particles located on optical holders and near optical components including various metals, organic compounds, glass, and fibers. The origin of these particles is not yet clear, but one can consider the classical contamination mechanisms such as during installation, from laser-induced damage, and from ghost beams. Additional contamination mechanisms specific to this type of lasers can be postulated. For example, the short-pulse lasers are often directly connected to the target chamber (no physical barrier), where exposure of target materials can produce contamination particles that can be transferred to sensitive optics, either directly for optical elements in the line of sight or via other mechanisms such as electrostatic mechanisms.[23] Furthermore, some systems are connected to a larger primary target or running in parallel with a fusion-class nanosecond laser system that produces significant fragmentation of targets and associated target holders. In such a setting, small pressure gradients (such as connecting different vacuum chambers or during compression and decompression) could transport particles from the main target chamber to optical components upstream.

The primary objective of this work is to investigate the relevant short-pulse laser–particle interactions that lead to damage initiation and/or secondary contamination at fluences significantly below the pristine laser-induced-damage threshold (LIDT). Several mechanisms are identified: localized field intensification by multibeam interference and particle microlensing, plasma scalding, secondary contamination by the generation of nanoparticles or fragments, and particle melting. The secondary objective of this work is to investigate the impact of additional pulses irradiating these sites. A second pulse upon damaged sites causes damage growth at fluences significantly below the pristine LIDT, whereas exposure of secondarily contaminated sites to additional pulses leads to additional damage.

2 Experiment

Four different types of particles were dispersed onto the surface of multilayer dielectric mirror samples to serve as a contamination model of materials typically found in the operational environment of large-aperture systems. The particle materials were stainless steel, borosilicate glass, low-density polyethylene (PE), and polytetrafluoroethylene (PTFE). This set of materials also

Table 1 Material properties of model-contaminant particles.

Material	Young's modulus	Melting point (°C)	Boiling point (°C)	Specific heat (J/°C · g)	Density (g/cm^2)	Refractive index	Shape
304 stainless steel	193 to 200	~1400	~2800	0.5	8	$\sim 3 + 4i$	Sphere
Borosilicate glass	64	~1600	~3000	0.83	2.5	1.51	Sphere
PE	0.8	~110	360	0.2	0.9	1.49	Sphere
PTFE	0.5	327	327	1.0	2.2	1.38	Random

represents a wide distribution of optical and thermomechanical properties (see Table 1). The experiments were performed with particles having nominal diameter of 40 μm, and all except PTFE were nominally spherical in shape. Downselection of the particles' size and shape for testing and analysis allowed a more repeatable and predictable interaction with which to extract relevant mechanisms. Although "real" contamination would involve particles of predominantly nonspherical shape and broader size distribution, the interaction mechanisms would be expected to be directly relevant, and the knowledge attained by these experiments should be translatable to an actual operational environment. We note that particles of this size and larger were found adjacent to optics in the aforementioned ongoing study of the OMEGA EP vacuum chamber.

The contaminated high-reflector samples of this work were irradiated in air at a 45 deg angle of incidence, *s* polarization, 1053-nm laser wavelength, and pulse duration of 0.6 or 10 ps. The commercially available multilayer dielectric mirror samples (20D20DM.10, Newport) were designed for reflection of this wavelength at 0 deg to 45 deg angle of incidence, which in this particular coating run used TiO_2 and SiO_2 in its outer layers. Using an *in-situ* microscope and translation stages, each particle was placed within 20 μm of the peak of the laser's 300-μm-diameter Gaussian spatial distribution. The particles were distributed sparsely enough on the sample such that only one particle interacted per test site. Each site was exposed to one laser pulse, representing the majority of the data in this paper, and a small subset was irradiated by an additional pulse as part of a preliminary study of the stability of the resulting morphology to repeated laser exposure. The test laser fluences were kept below the one-pulse pristine LIDT (measured beforehand), where pristine refers to the high-reflector sample without any contamination particles. Since the particles (selected by the on-line microscope system) for laser irradiation had a nearly identical size and shape (except PTFE), the observed interaction behaviors were highly reproducible, and therefore the results at different sites could be directly compared. The resulting morphology of the sites was characterized with various techniques, including differential interference contrast (Nomarski) microscopy, atomic force microscopy, and scanning electron microscopy.

Additional details on the experimental procedures and evaluation of the resulting LIDT, particle ejection thresholds (laser cleaning), and a preliminary assessment of mechanisms involved have been presented elsewhere.[22]

3 Results

The irradiation of all particle types caused damage of the coating at significantly lower fluence compared with the pristine (not contaminated) coating. Figure 1 summarizes the absolute LIDT values, and Table 2 shows the normalized values compared with the pristine coating LIDT. Overall, the presence of particles caused a reduction of threshold by at least a factor of 4 and up to two orders of magnitude. Note that the fluence in Fig. 1 is plotted in a logarithmic scale to accommodate this wide range of values. The reported LIDT values correspond to a 50% probability of damage, and the upper and lower bars represent the measured 100% and 0% damage probabilities, respectively.

The LIDT under exposure to 10-ps pulses exhibited a higher value than the 0.6-ps pulses, as expected. However, the noteworthy result is that the relative change of the LIDT with respect to the pristine coating is approximately the same (within uncertainty) for both pulse durations

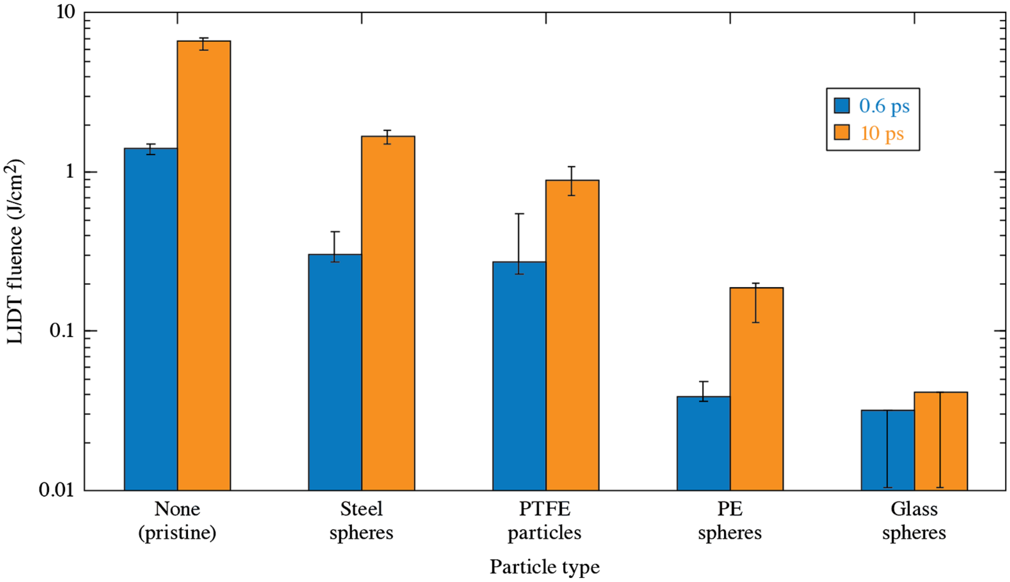

Fig. 1 LIDT fluence for ablation of the mirror in the presence of a given particle.

Table 2 LIDT reduction factor in the presence of particles.

Pulse duration	Steel	PTFE	PE	Glass	Pristine LIDT (J/cm^2)
0.6 ps	$4.6^{+0.6}_{-1.2}$	$5.3^{+1.0}_{-2.7}$	37^{+3}_{-7}	>45	1.4
10 ps	$4.0^{+0.4}_{-0.5}$	$7.5^{+2.0}_{-1.2}$	36^{+24}_{-2}	>160	6.7

(see Table 2). This suggests that the laser–particle interaction mechanisms are similar (if not identical) for both pulse durations tested.

In the case of glass microspheres, an upper-bound LIDT is reported because damage occurred at fluences below those required to remove (separate from the surface) the particle; therefore, it was not detectable with the on-line system. Furthermore, during sample analysis, we discovered that all glass-interaction sites generated damage, so the lower-bound LIDT value was extended. This uncertainty implies that the LIDT reduction factor for glass (Table 2) is reported as a lower-bound as well. Nonetheless, the glass spheres were measured to have the lowest damage thresholds with a single laser pulse compared with other particle types.

As will be discussed in the subsequent sections of this paper, the observed LIDT behavior with the various model-contaminant particles has been identified to be caused by localized intensification of the laser impinging on the coating by one of two mechanisms: (1) multibeam interference (Sec. 3.1) or (2) microlensing by the particle (Sec. 3.2).

Besides damage (localized ablation) that was initiated by the electric-field intensification on the mirror surface, electric-field intensification occurs on/inside the particle, and its subsequent melting, ablation, and/or fragmentation caused additional modifications. These modifications included the generation of secondary contamination by nanoparticles, particle fragments, and liquid jets (Sec. 3.3), as well as scalding of the coating due to the formation of a plasma plume (Sec. 3.4).

3.1 *Damage Due to Beam Interference*

The laser interaction with reflective particles was observed to generate damage on the mirror that could be interpreted to arise from an interference pattern, generating localized intensification. Figure 2(a) shows an example of the damage morphology generated by steel particles under exposure to 0.6-ps pulses, formed significantly above the particle-induced LIDT, where the ripples of ablated coating indicate that the local fluence oscillated above and below the LIDT of the

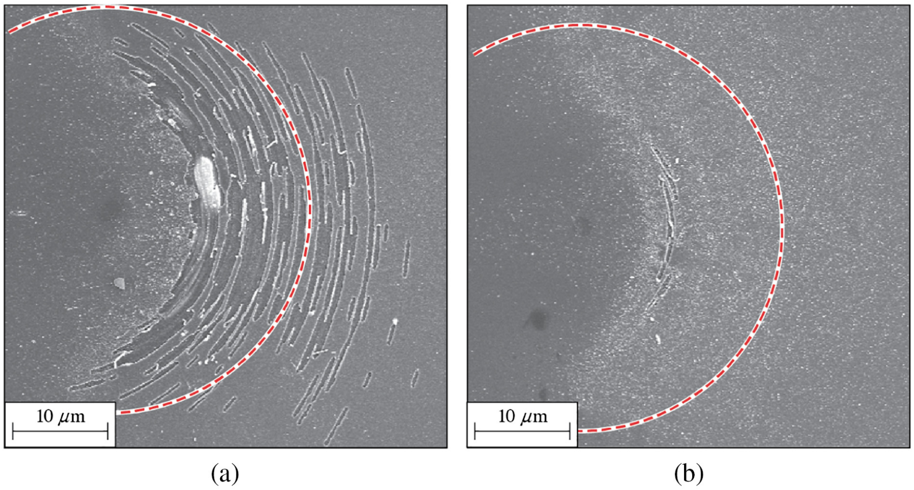

Fig. 2 SEM of damage sites resulting from the interaction between a stainless-steel microsphere and 0.6-ps pulse at fluence (a) 1.1 J/cm^2 and (b) 0.4 J/cm^2. The approximate initial location of particle is shown (dashed line), and the laser was incident from right at a 45 deg angle of incidence.

pristine coating. For comparison, the site in Fig. 2(b) was formed by a fluence nearer to the particle-induced LIDT, and only a single damage ripple is formed, presumably corresponding to the region of peak intensification. The ripples were always observed near the particle's initial location on the same side as the laser incidence. The approximate initial location of the particle is shown in Fig. 2 with a dashed line, and the laser was incident from the right side at a 45-deg angle of incidence.

The cause of this interference pattern is the set of multiorder reflections that are created between the particle and the mirror surface. For this experiment at a 45-deg angle of incidence, there are five orders of reflection that interfere with the directly incident beam. Figure 3(a) shows a ray that is directly incident upon an arbitrary point on the mirror, and Figs. 3(b)–3(f) show the five other rays that eventually intersect that same point with some phase delay. Since the majority of the intermediate reflections occur from the surface of the particle, significant intensification (and reduction of LIDT) must require a particle material with high reflectivity. This is consistent with our observations of ripples as the dominant damage feature with the steel particles, which are metallic and exhibit high reflectivity at all angles of incidence.

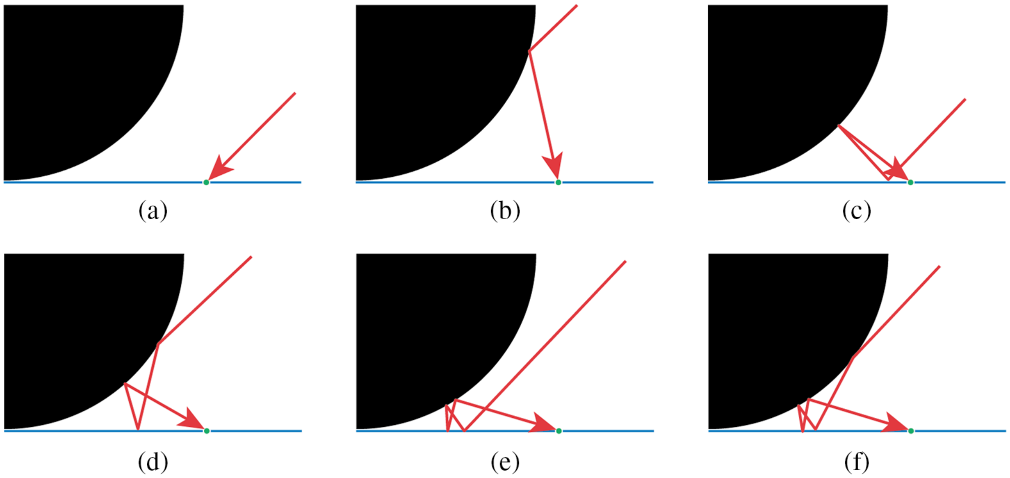

Fig. 3 Set of ray diagrams that demonstrate how multiorder reflections are generated between the reflective particle (black) and mirror plane (blue). All of these rays (red) eventually intersect at the green dot after some number of reflections: (a) 0, (b) 1, (c) 2, (d) 3, (e) 4, and (f) 5.

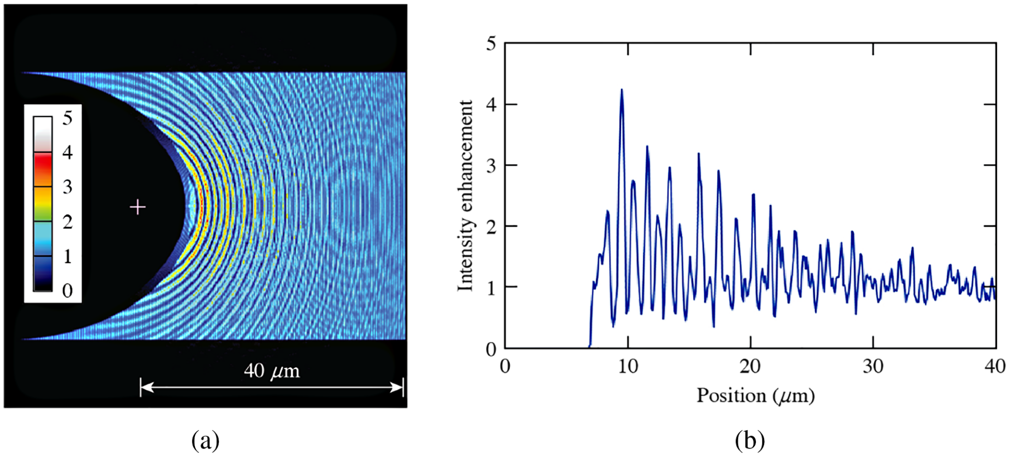

Fig. 4 (a) Interference pattern for a reflective sphere on a mirror, simulated by 3-D ray tracing. Intensity is in units of enhancement, where 1 corresponds to incident intensity. (b) The lineout is taken along the horizontal axis, with zero at the particle center (pink "+").

To quantify the intensification caused by this interference pattern, we performed three-dimensional (3-D) ray-tracing simulations of this interaction. The simulations were performed by a coherent ray-tracing code implemented in Interactive Data Language. While conventional ray tracing simply adds the intensity of each ray, coherent ray tracing instead keeps track of both the amplitude and phase of each ray for the duration of the simulation, and then the intensity pattern was obtained by squaring the complex amplitude at each point along the mirror surface. A typical run had about 10^6 rays that resulted in several hundred rays per square wavelength. For simplicity, the spherical particle and plane mirror were both assumed to have a perfect reflecting boundary. Other conditions were assumed the same as in the experiment. Figure 4 shows the results of these simulations, where the intensity values are plotted as an enhancement factor, i.e., in units of the incident laser intensity I_0 with no particle present. The peak enhancement value is about 4.3 and is located on-axis 9.5 μm from the sphere's point of contact with the optic. The local maxima of the interference pattern decay nonmonotonically with increasing distance from the particle, until reduced to the base value of 1. The ripple period is not well defined, but the strongest spatial frequency along the central axis is 0.97 μm.

These interference patterns resulting from the simulation reasonably reproduce the ripples of ablated coating observed in the experimental results. Although the ablated regions of adjacent peaks sometimes merge together, partially disguising the underlying pattern, the sickle shapes and periodicity confirm that these features are due to the reflections from the sphere. Furthermore, a dark smudge can be seen in Figs. 2(a) and 2(b), which corresponds to the point of contact of the sphere and matches the calculated 10-μm distance from the leftmost ripple. Most importantly, the simulated enhancement factor (4.3) matches the LIDT reduction factor measured in experiment (4.0 and 4.6, Table 2). Although the calculations are based on a very specific particle size and shape, these results have the important implication that the LIDT reduction due to reflective particles can be accurately predicted for short pulses for a known particle geometry. It is well documented in short-pulse laser damage of dielectric coatings that the damage initiation location within the stack is directly correlated to the pattern of electric-field intensity.[24] The present results are consistent with this concept.

This type of ripple pattern was also observed with transparent particles, such as glass, but at much larger fluence (∼2×) because the Fresnel reflection coefficient is much lower ($r \ll 1$ for the particle surface). Considering the rays of Fig. 3, the contributions of Figs. 3(b) and 3(c) are proportional to r and Figs. 3(d)–3(f) are proportional to r^2 or r^3. Therefore, it is not surprising that intensification by interference was not the LIDT-governing mechanism for the glass and plastic particles (see Sec. 3.2).

The reflectivity of the optic surface also contributes to the strength of the interference pattern. Since the optic in this experiment was highly reflective ($r \approx 1$) over a broad range of incidence angles (0 deg to 45 deg), all orders provided approximately their full contribution to the total electric-field amplitude. For example, a similar intensification pattern would be expected for a metallic particle on a metal mirror, which also exhibits high reflectivity for a broad range of angles of incidence. In contrast, however, a metallic particle on a transparent window or multilayer dielectric mirror with narrower solid angle of high reflectivity would have a reduced and modified interference pattern, following a similar analysis to the glass-on-mirror description above.

3.2 *Damage Due to Microlensing*

Microlensing by transparent particles generated the lowest LIDT values observed in this work. This is due to the strong intensification caused by the transparent spherical particles behaving as a ball lens. Figure 5(a) shows a two-dimensional (2-D) ray diagram for a transparent sphere of refractive index $n = 1.5$.

Rays incident at larger radii undergo significant aberration, seen by the rays that do not converge, but the majority of the rays focus on a spot only a few microns in diameter. This focal-spot induced damage at fluences two orders of magnitude below the pristine coating LIDT. A typical example is shown in Fig. 5(b), where the particle still remains on the surface next to the small ablation crater, which is partially obstructed from view.

Ray-tracing simulations are not adequate to calculate the intensification factor caused by the microparticle lensing because ray density exceeds the diffraction limit and therefore significantly overestimates the peak intensity (by more than an order of magnitude in this case). However, an upper bound of the intensification was calculated by determining the intensity of an Airy disk that would be produced for these dimensions and illumination conditions. First, we assume constant fluence ϕ_0 incident across the sphere, which is reasonable since the particle diameter ($d = 40\ \mu\text{m}$) is much smaller than the incident beam size (300 μm). The particle's aperture collects a total energy of $E_0 = \phi_0 \pi d^2/4$, but some of that energy will be diverted by Fresnel reflection from the sphere, which in this case approximately corresponds to a throughput of $\eta_F = 0.82$ (calculated by ray tracing). The peak fluence of an Airy disk focused by a lens is given by $\phi_A = E_0 \pi d^2 / 4\lambda^2 f^2$, where the focal length of the sphere is given by $f = nd/4(n-1)$. Therefore, the peak enhancement factor is given by $\phi_{\text{enh}} = \phi_A/\phi_0 \approx \eta_F(\pi d^2/\lambda f)$. Using the values for this experiment, $n = 1.5$ and $f = 30\ \mu\text{m}$, the upper bound of the enhancement from the transparent sphere is estimated to be $\phi_{\text{enh}} < 1300$. Note that simple geometry shows that the distance to the optical surface from the sphere's center is $d/2 \cos\theta \approx 28.3\ \mu\text{m}$, which means that the best focus is just beneath the surface by $\sim 1\ \mu\text{m}$ once the angle of incidence is considered.

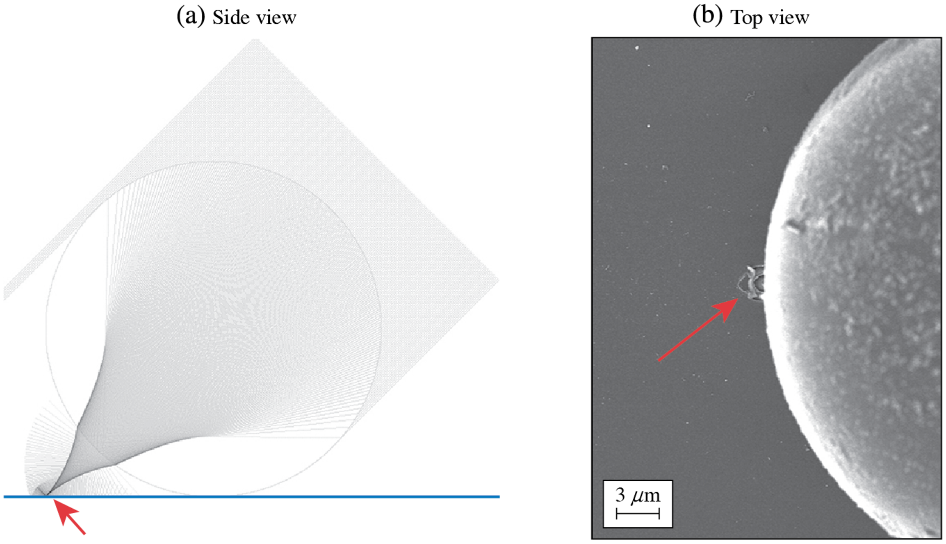

Fig. 5 (a) A 2-D ray diagram of a transparent spherical particle on a plane, and (b) a SEM of a damage site induced by this intensification. The particle was not removed at this low fluence (32 mJ/cm^2). The arrows indicate the location of peak intensification and damage. The laser was incident from the right at a 45-deg angle of incidence.

Several effects can decrease ϕ_{enh} from that upper estimate. First, any losses and aberrations due to the imperfections of the real spherical particle's surface or shape will decrease the enhancement. This would be especially relevant when considering the varied shapes of real contamination particles. Second, the tight focusing geometry will cause a slight polarization mixing in the focal plane, but we do not expect a significant decrease to the peak intensity. The most important contribution may be the spherical aberration, which will significantly degrade the quality (and therefore peak intensity) of the focal spot. This aberration causes a phase error of ~ 1.2 rad for a sphere of 40λ diameter. Using this phase error to calculate the Strehl ratio, the spherical aberration causes a further peak-intensity reduction by approximately a factor of 6.8. The final estimate of the enhancement by microlensing is then $f_{\mathrm{enh}} \approx 190$. In addition, as the localized intensity increases, an array of nonlinear processes can be activated that can lead to nonlinear absorption and ultimately damage initiation inside the particle as well.

The experimentally measured LIDT values are consistent with the above calculation, suggesting an enhancement factor of at least 160, as seen for glass particles in Table 2. However, the enhancement factor for PE spheres is significantly less, despite also being a nominally transparent sphere with similar refractive index. The cause of this difference is likely due to significant nonlinear absorption in the PE, such that an estimate of the total absorption is given by $A \approx (f_{\mathrm{enh}} - f_{\mathrm{enh,measured}})/f_{\mathrm{enh}}$. Given the variability of the measured enhancement factor, this corresponds to 70% to 80% of the beam energy to be absorbed within the <40-μm propagation distance. Although the PTFE may also undergo significant nonlinear absorption, a similar estimate cannot be made quantitatively from the damage data because the irregular shape of the PTFE particles also leads to significant reduction of enhancement factor due to optical aberrations.

In all cases, the ablation crater morphology is similar among all three transparent particle materials used in this work (shown in Fig. 6) after adjusting for the significant difference in fluence levels. All craters have a diameter ≤ 3 μm, consistent with focusing onto the optic with

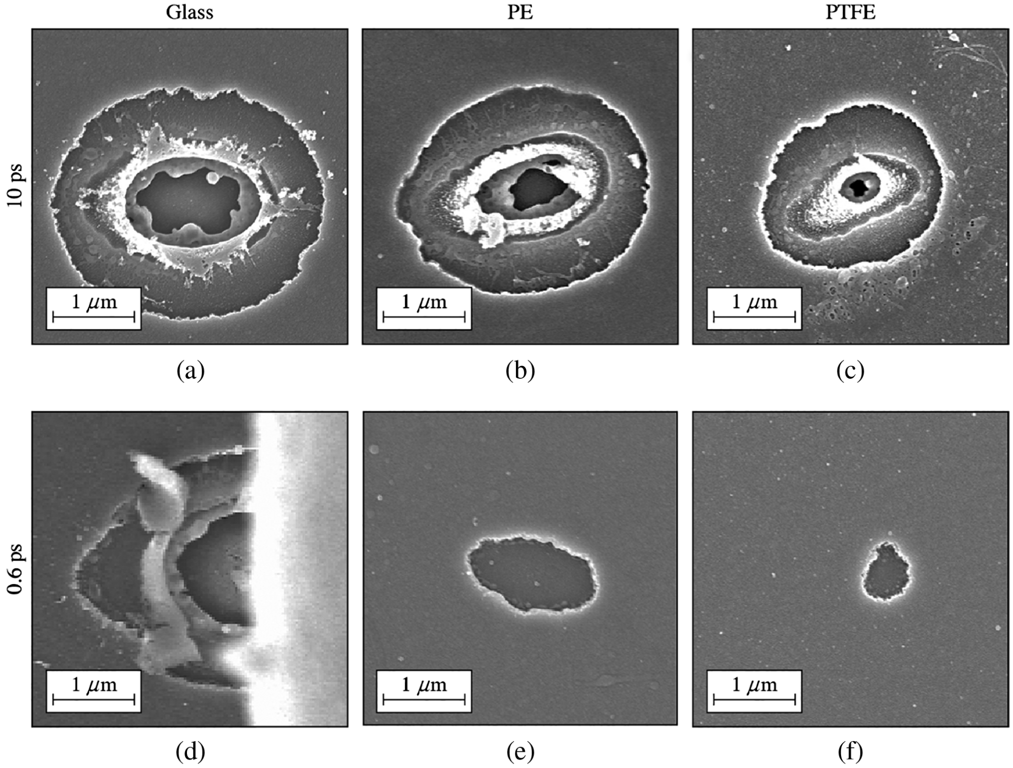

Fig. 6 SEM images of ablation sites formed by laser incidence at the indicated pulse duration on a transparent microsphere of indicated material. Respective fluences were (a) 56, (b) 190, (c) 720, (d) 32, (e) 47, and (f) 200 mJ/cm^2. An unremoved microsphere partially obscures site (d). All images have the same length scale.

large numerical aperture. With 10-ps pulses [Figs. 6(a)–6(c)], damage was observed to penetrate beneath the first layer, even near the LIDT fluence. With 0.6-ps pulses [Figs. 6(d)–6(f)], only the outer layer ablated near the LIDT fluence. The results for glass in Fig. 6(d) clearly show that $32\ \mathrm{mJ/cm^2}$ incident on the glass sphere was still far above the 0.6-ps LIDT, indicated by the crater, which is wider and penetrates deeper than the craters formed by other transparent particles near their respective LIDT's. In addition, a portion of the glass microsphere can be seen to obscure half of the crater from the SEM's view [bright blur on the right of Fig. 6(d)] since the microsphere was not removed at that low fluence. The craters formed by an interaction with PTFE particles were more irregularly shaped [Figs. 6(c) and 6(f)] and required higher fluence to initiate, which are consistent with the more irregularly shaped particles and decreased symmetry for microlensing. The reduced severity of damage in Figs. 6(e) and 6(f) in comparison with Figs. 6(b) and 6(c) may be consistent with screening inside the particle due to increased nonlinear absorption of the shorter pulse (with correspondingly higher intensity). All of the above indicate that damage initiation on the coating induced by transparent particles arises by particle microlensing.

3.3 *Secondary Contamination*

The interaction of the particles with the laser beam not only leads to damage on the coating (discussed in the previous section) but also gives rise to significant energy deposited onto the contaminant microparticle. Specifically, the laser fluence/intensity can initiate damage on the surface or inside of the particle itself, producing plasma formation as well as melting and fragmentation of the particles in some cases. This process has a potential to distribute secondary contamination across an area even larger than the area that particle originally occupied, along with potential modification of the coating's top layer(s). Although secondary contamination is not strictly damage of the coating, it can effectively be a damage precursor locally or on downstream optics due to modulation of the beam profile during subsequent exposure. Previous studies of secondary contamination have been performed with nanosecond pulses, where metallic particles were predominantly observed to spread liquefied material[17] whereas glass particles were observed to fragment.[14] Our observations of secondary contamination with short pulses involved liquid splatter, microparticle fragments, and nanoparticles, but the conditions and morphologies significantly differed from published results in the nanosecond-pulse regime. The type and quantity of the secondary contamination was largely a function of the model-contaminant's material properties (see a subset of relevant physical properties in Table 1).

The dominant type of the secondary contamination generated by stainless-steel particles was nanoparticles, and they were observed for all other particle types, although in lesser quantity. Nanoparticles are known to be generated by short-pulse laser ablation of basically any material,[25–27] caused by material superheating, which initiates a material response that is more rapid than thermal diffusion and material expansion time scales, limiting the size of droplet formation.[28] As can be seen in Figs. 7(a)–7(b), the steel droplets deposited onto the mirror by 0.6-ps pulses were ≤ 100 nm in diameter. In fact, the long central object in Fig. 7(b) is actually an agglomerate of many particles with diameters on the order of 10 nm. We note that the formation of these nanoparticles is clearly distinct from the prevailing mechanism for nanosecond pulses with metals: microscale liquid droplets. This difference is attributed to the initial condition during material superheating, namely the initial peak temperature and pressure.

Figures 7(c)–7(e) show that the nanoparticles are deposited preferentially on the laser-incident (right) side where the peak intensification occurs for reflective particles, as discussed above in Sec. 3.1. Just as an interference pattern of ripples is formed on the coating, a corollary set of ripples is formed on the particle, which creates a pattern of increased fluence and intensity that locally initiates ablation of the surface of the particle. The expanding ablation plume then deposits particles onto the optic, and with sufficient momentum transfer can cause ejection of the microparticle itself from the optic.[15] The SEM image in Fig. 8(a) shows ablation ripples on a steel microsphere that was irradiated by 10 pulses, spreading nanoparticles onto the surface without removal of the microsphere. Due to the observation direction of the SEM image, only the ripples on the top side of the particle are shown, although it demonstrates the effect due to the presence of two-beam interference in that region. The multibeam interference occurring on the underside

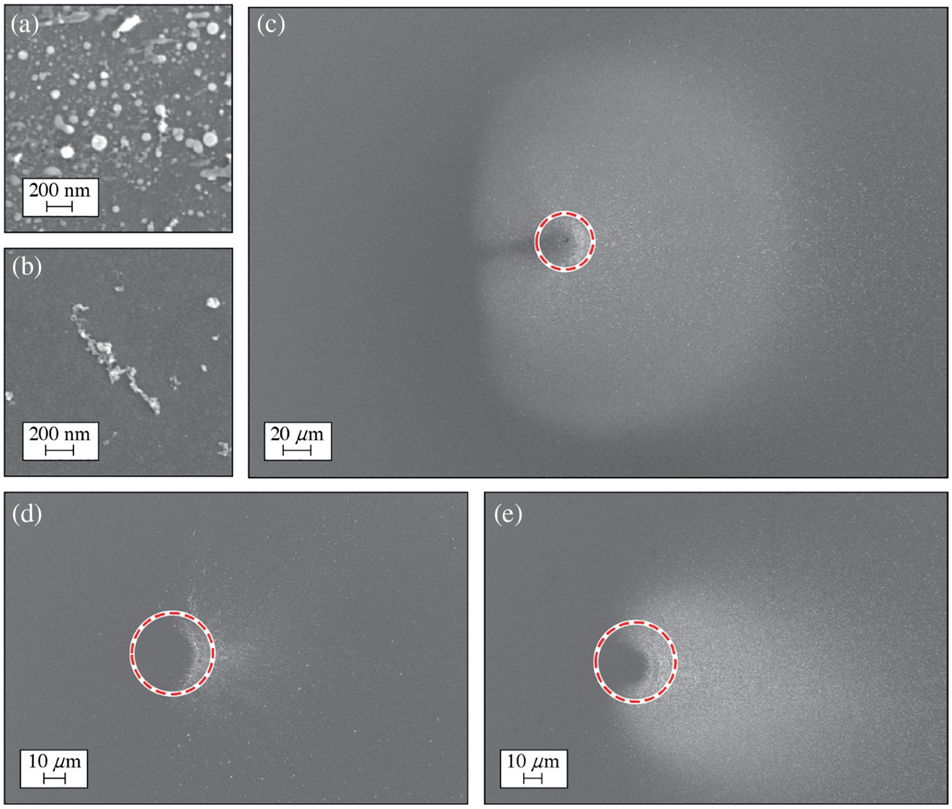

Fig. 7 SEM images of secondary contamination generated from a steel particle, with initial particle location shown in red dashed line and the laser incident from the right. (a) Densely contaminated region, (b) agglomerate of nanoparticles in sparsely contaminated region, (c) 10 ps, 1.4 J/cm^2, (d) 0.6 ps, 0.2 J/cm^2, (e) 0.6 ps, 0.2 J/cm^2, 10 pulses without particle removal. The laser was incident from the right at a 45-deg angle of incidence.

is visualized in Fig. 8(b) by plotting a 2-D projection of the intensity calculated using the ray-tracing simulations discussed earlier. However, this raw data must be rescaled due to the curvature of the sphere. Although the lateral resolution of the grid is fixed at 0.1 μm, pixels farther from the point of contact correspond to a larger area of the sphere's surface, so the pixels of Fig. 8(b) must be multiplied by cos θ to represent the intensity on the surface (where θ is the angle from the point of contact). At angles $\theta > \sim 75$ deg, the pixel size of the simulation passes the Nyquist limit of the expected fringe period, so the data should be ignored. The lineout of the central axis [Fig. 8(c)] has been rescaled following the above and has a magnitude of the right-most peak set to the known two-beam interference peak value of 4. This shows that ripples of significant field enhancement also occur on the underside of the sphere, although they do not surpass the intensification of the two-beam interference maximum. We additionally note that surface plasmons or surface plasmon polaritons may be excited on the metal particle surface due to imperfections/roughness, contributing to and potentially modifying the interference pattern on the particle. However, for the scope of this work with particles of size larger than the laser wavelength, this process is not expected to affect the distribution of intensity on the optic.

The nanoparticles are deposited over a distance of tens to hundreds of microns from the particle, depending on laser fluence. Importantly, this deposition is observed to occur at very low fluences, below those required to initiate coating damage from multibeam interference or ejection of the particle, as is the case for all of the images in Fig. 7. Since the LIDT of the metal particle is relatively independent of pulse duration in this regime (because linear absorption is the dominant energy deposition mechanism), the 10-ps pulses can deliver much larger fluences without damaging the coating but produce increased density and/or area of contamination [compare Figs. 7(c)–7(d)]. However, secondary contamination at lower fluences can still be relevant because it can accumulate, with increasing number of pulses, a layer of absorbing nanoparticles

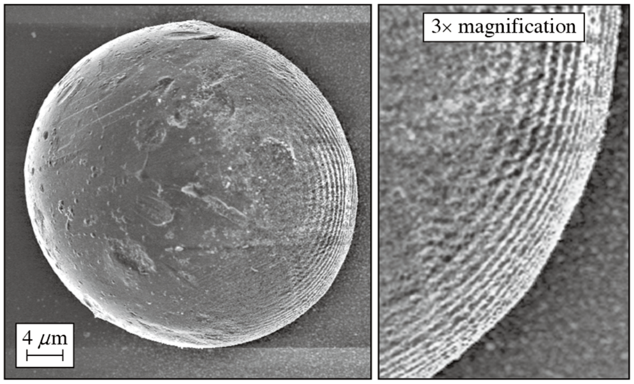
(a) Top view

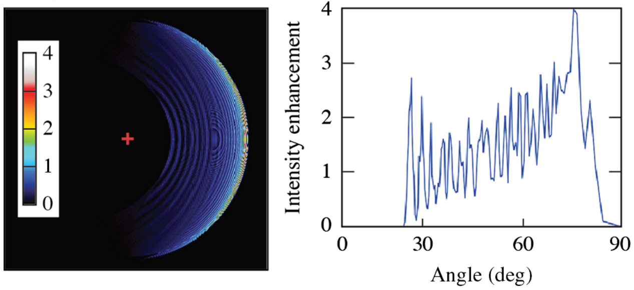
(b) Bottom view

(c)

Fig. 8 Examples of the interference pattern that occurs on a reflective particle. (a) The SEM shows damage ripples on a particle that was not removed by the laser after ten pulses at 0.2 $\mathrm{J/cm^2}$. (b) Underside view of raw ray density pattern on such a particle, calculated by the 3-D ray-tracing simulation from Sec. 3.1. (c) The central lineout starting from the pink cross is rescaled to account for the nonuniform binning across the sphere surface, showing the approximate intensity enhancement. Data at angles >75 deg are beyond the Nyquist limit and should be ignored.

in the surrounding area (while the initial particle does not acquire sufficient recoil momentum to be removed by this interaction and therefore terminate the deposition process). For example, compare Figs. 7(d) and 7(e), which were formed at the same fluence under exposure to 1 or 10 pulses, respectively, while the particle was otherwise unaffected by the laser beam (the steel microsphere was removed by nonlaser methods before the SEM imaging). Each laser pulse generated a new plume of nanoparticles, leading to film-like accumulation similar to the method of pulsed laser deposition of thin films.

Laser energy could also be deposited directly onto the bulk of transparent particles via microlensing due to the partially converged beam near the exit surface. Although the peak enhancement from microlensing occurs beyond the particle and near the optical coating, significant enhancement also occurs inside the particle near the beam exit surface. Finite-difference time-domain simulations of this near-exit-surface enhancement have been calculated previously for 20-μm-diameter fused-silica spheres and 351-nm laser wavelength,[14] showing enhancement peak values reaching $\approx 13\phi_0$ (where ϕ_0 is the input fluence). Using a similar analysis to Sec. 3.2, the relative change in the beam area at the exit surface is given by $(2-n)^2/n^2$. Then, the on-axis enhancement $\phi_{\mathrm{exit}} = \eta_F n^2 \phi_0/(2-n)^2 \approx 8\phi_0$, assuming lossless linear optics. Obviously, the discussion of secondary contamination via material ablation requires nonlinear absorption and violates this assumption, but enhancement of one order of magnitude is a reasonable approximation near the onset of near-exit-surface ablation in the bulk of the particle.

For the glass microspheres, near-exit-surface ablation was not observed until the fluence was well above the particle-induced LIDT. This is consistent with the calculations of intensification due to microlensing (see Sec. 3.2) that predict an intensification factor that is ∼24× larger on the coating than on the particle's exit surface. Nonetheless, near-exit-surface ablation is still observed for fluences far below the pristine coating LIDT. In addition to the nanoparticles from

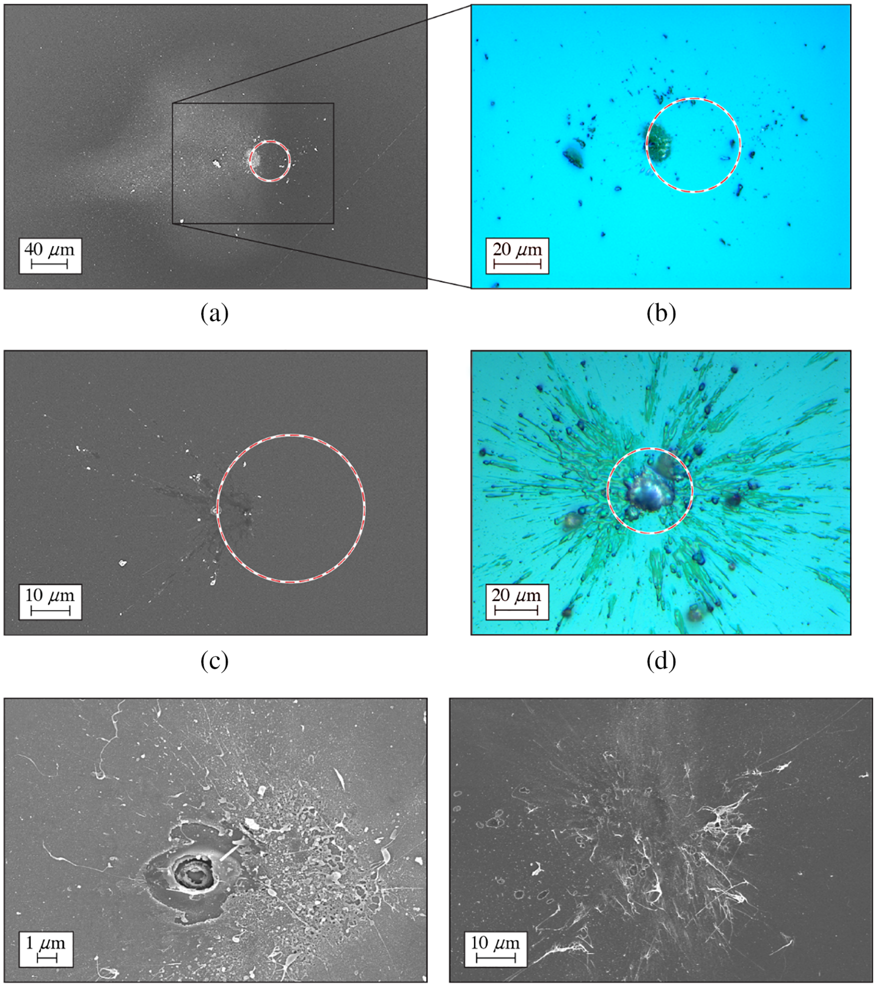

(a) (b)

(c) (d)

(e) (f)

Fig. 9 SEM and Nomarski micrographs of secondary contamination with initial particle location shown in red dashed line and laser incident from the right. (a), (b) Glass, 10 ps, 0.55 J/cm^2, respectively; (c) PE, 10 ps, 0.19 J/cm^2; (d) PE, 0.6 ps, 0.79 J/cm^2; (e) glass, 0.6 ps, 1.0 J/cm^2; and (f) PTFE, 0.6 ps, 1.0 J/cm^2. The laser was incident from the right at a 45-deg angle of incidence.

the ablation plume, the pressure generated inside the particle leads to its fragmentation, similar to the process reported for nanosecond pulses.[14] The contaminated sites were also found to have some glass nanofibers with microscale lengths, evidence of high-speed molten material ejection present in the plume. However, the small total volume of the fibers is not considered to be impactful.

Considering the impact of the secondary contamination, the nanoparticles of transparent materials were relatively less impactful than the metal nanoparticles. The simplest reason is the difference in optical properties between metals and dielectrics. A collection of subwavelength metal particles can still undergo significant absorption and reflection due to a nanoscale skin depth, whereas subwavelength transparent particles change the amplitude and phase of the light by very little, perhaps causing a slight localized increase of scatter. On the other hand, microparticle fragments (larger the laser wavelength) composed of dielectric materials are able to significantly alter the beam propagation characteristics. For example, compare the images in Figs. 9(a) and 9(b), which show SEM and Nomarski micrographs of the same site formed by interaction with a glass microsphere. The SEM image [Fig. 9(a)] shows the large region that contains nanoparticles (manifested as an area of SEM-contrast increase), similar to the results with steel particles [compare Fig. 7(c)]. However, this same region of deposited nanoparticles is not detected with Nomarski microscopy [Fig. 9(b)], whereas the microparticle fragments (and the central damaged region) are obvious. The nanoparticles and fragments also can be propelled much farther away, even though our experiment did not quantify this.

The dominant secondary contamination mechanism observed for the PE microspheres is splattering of liquefied material, owing to its significantly lower melting temperature. Examples are shown in Figs. 9(c) and 9(d). Specifically, Fig. 9(c) shows the remnants of a jet-like ejection of material from the particle near the location of the beam exit, which was formed by an incident fluence of only 3% of the pristine coating LIDT. At higher fluences such as Fig. 9(d) (which had fluence >50% of pristine LIDT), absorption throughout the particle causes the particle to disintegrate, splattering liquid and large fragments in all directions. In fact, a large segment of the particle remains on the surface approximately in its initial location.

PE particles clearly cause the greatest volume of secondary contamination material. The damage site due to particle microlensing is still visible in both Figs. 9(c) and 9(d). However, the impact of the secondary contamination is arguably the greater concern for PE particles. The observed contamination morphologies of PE were approximately the same at both pulse durations (after scaling fluence by fraction of LIDT), except that 0.6 ps showed a slight preference for fragmentation over melting. This is likely again due to the different initial pressure and temperature conditions caused by decreasing the pulse duration.

The randomly shaped PTFE particles produced secondary contamination morphologies that were qualitatively between the results from PE and glass, which is consistent with its intermediate melting point temperature. The majority of the contamination was observed to be in filaments or strands of material, but significantly less total volume than for PE but more than for glass. This can be concluded by examining Figs. 9(d)–9(f), which show a site from each transparent particle material at a fluence in the range 60% to 70% of the 0.6-ps pristine LIDT. Filaments and/or splatter can be seen in all three cases, but the images show significantly different length scales. The results suggest that the amount of generated liquefied secondary contamination is correlated to the melting temperature of the transparent material. It is worth noting that there are many damage initiation sites generated by a single particle in Fig. 9(f), which may be a more problematic consequence for PTFE than secondary contamination.

3.4 *Plasma Scalding*

Plasma-induced etching (commonly referred to as plasma scalding) is manifested as a surface discoloration under Nomarski microscopy and has been reported previously as one of the most commonly observed damage mechanisms of thin films by nanosecond pulses.[29–31] In those reports, the mechanism is explained as involving damage initiation on the coating that provides seed electrons to an avalanche ionization process in the surrounding air, which then forms an expanding ionization front for the duration of the laser pulse.[29,32] The air plasma undergoes strong laser absorption, becoming very hot, depositing some of that energy to the optic surface, and causing it to overheat, etching away some material. After being rapidly cooled following the interaction, the resulting outer surface is covered by nanoscale bubbles and/or pits, such that it optically appears to be "scalded." As pulse duration is decreased, the area of the scalded region also decreases due to decreased time for the lateral growth of the air plasma. In fact, scalding has been reported to be absent for 260-ps pulses[29] due to the lack of time for the entire mechanism to sufficiently develop.

In contrast, we have observed in this work significant (particle-) contamination-induced plasma scalding with 10-ps pulses, as shown in Fig. 10, which suggests that the mechanism is different. The cause of short-pulse scalding is believed to be not due to an air plasma, but instead due to the plasma plume of ablation that expands from the particle and then interacts with the optic. Consider Fig. 10(a), which shows a scald formed adjacent to the ablation crater. Clearly, the laser directly generated a crater (due to microlensing) in the expected location, but the material is scalded in a region that did not directly have laser irradiation. Therefore, an air plasma could not have been ionized in that region. Instead, the exit surface of the glass ablates and expands, within a narrow expansion cone from the normal to the particle's surface, toward the general direction of the ablation crater that simultaneously forms on the optic. However, the region to the right side of the crater is closer to the particle surface, thereby partially confining the

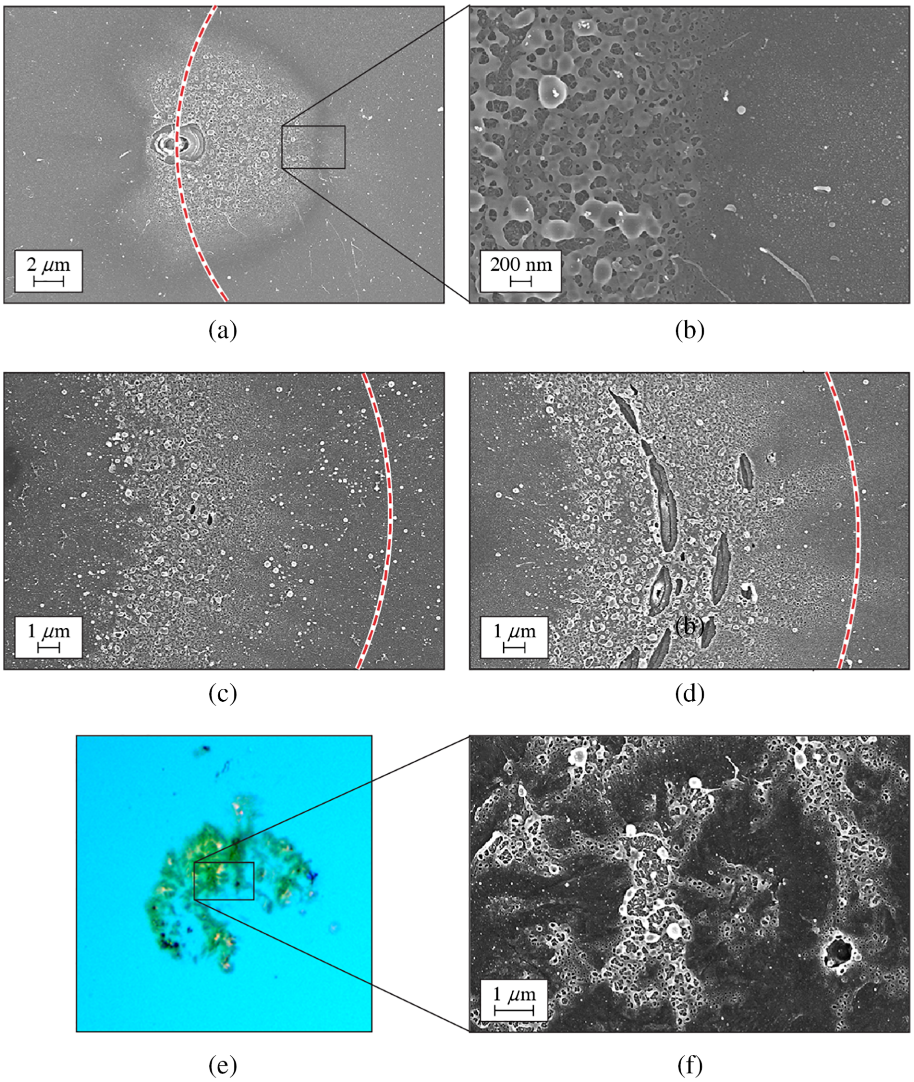

Fig. 10 SEM images of scalding with 10-ps pulses incident on a microparticle. (a), (b) Glass, 0.37 J/cm^2, (c) steel, 1.4 J/cm^2, (d) steel, 2.3 J/cm^2, (e), (f) PTFE, 2.2 J/cm^2.

plasma that maintains (due to reduced expansion) higher temperature and density over a longer period of time. While this plume is in contact with the coating, the heating of the interaction region produces a scald morphology (which is more pronounced on the right side of the ablation crater due to partial confinement of the plasma) that, on the nanoscale, is similar to previous published works using nanosecond pulses. In the case example using this work, nanoscale bubbles and voids are produced on the TiO_2 layer, which appeared greenish in our Nomarski microscopy [Figs. 9(b) and 10(e)]. See Fig. 10 for additional examples of plasma scalding formed by interaction with steel and PTFE particles. However, PE was not observed to produce scalding.

The morphology also appears to have imprinted some aspects of the ablation dynamics from the optic by influencing the scald pattern. Figures 10(c) and 10(d) show scalds that were formed at fluences below and above the particle-induced LIDT, where the scald region is located almost exclusively underneath the top-down area covered by the particle. In Fig. 10(c), the radial extent of the scald is approximately uniform, but in Fig. 10(d), the particle's plume appears to have collided with the plumes expanding from damage on the coating to create a nonuniform distribution where some of the coating ablation regions (right) appear to have partially shadowed the formation of the scald. This is also apparent in Fig. 10(a) where the left central region is arguably shadowed.

In any case, the scalding by short pulses observed in this experiment appears to be confined to the immediate vicinity of the particle, presumably scaling with its size and shape. Therefore, scalding with short pulses does not carry the risk of directly modifying large areas of the coating, as it does with nanosecond pulses. We did not observe significant scalding with the 0.6-ps pulses.

3.5 *Vulnerability to Subsequent Pulses*

The damage and secondary contamination features described in the previous sections may act as precursors to subsequent interactions with laser pulses. To preliminarily survey the potency of these features, we performed double-pulse exposure experiments. The results suggest that the initial damage site can grow or generate additional damage features following the exposure to the second pulse. Secondary contamination was observed to either remain on the surface, or be partially removed from the surface, but this is often accompanied by the generation of new damage sites and/or scalding. Characteristic examples of these dual-pulse interactions are shown in Figs. 11 and 12.

Damage growth from existing ablation craters is one major effect, and it is particularly prominent for 0.6-ps pulses. Figures 11(a) and 11(b) (different sites) show a comparison of one pulse versus two pulses for a steel particle site at a fluence ~36% of the pristine coating LIDT. The first pulse [Fig. 11(a)] generated a sickle-shaped ablation feature due to multibeam interference effects. The second pulse caused a widening of the existing ablation crater and forms ripples (consistent with previous work on damage growth with short pulses[33]) in an area that was completely shadowed by the particle during the first pulse. The results are similar for glass particles at

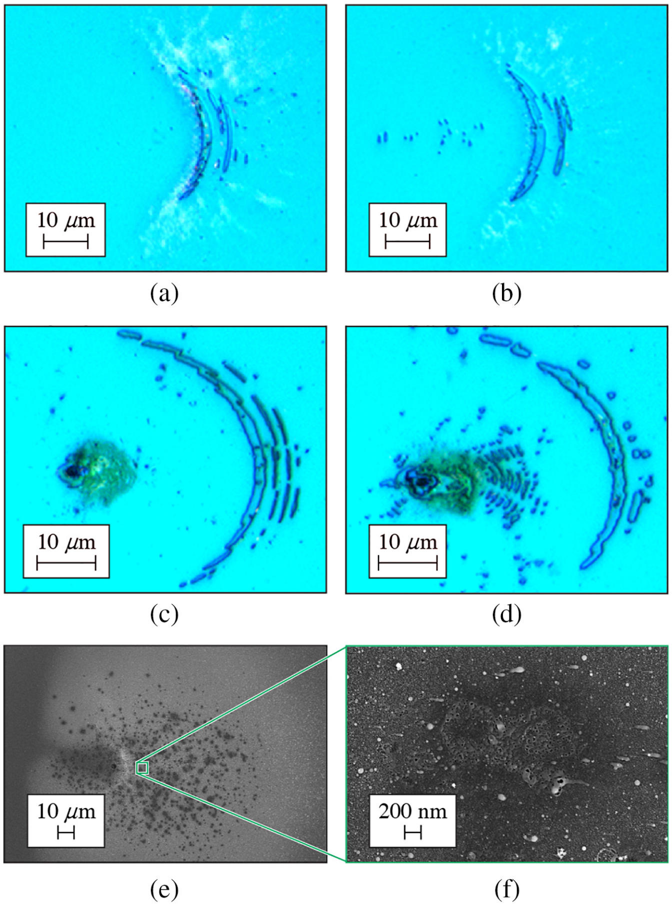

Fig. 11 Site morphology of one- and two-pulse exposures. Parameters: (a), (b) one and two pulses, respectively, steel, 0.6 ps, 0.5 J/cm^2, (c), (d) one and two pulses, respectively, glass, 0.6 ps, 0.9 J/cm^2, (e), (f) steel, 10 ps, 1.4 J/cm^2. The laser was incident from right at a 45-deg angle of incidence.

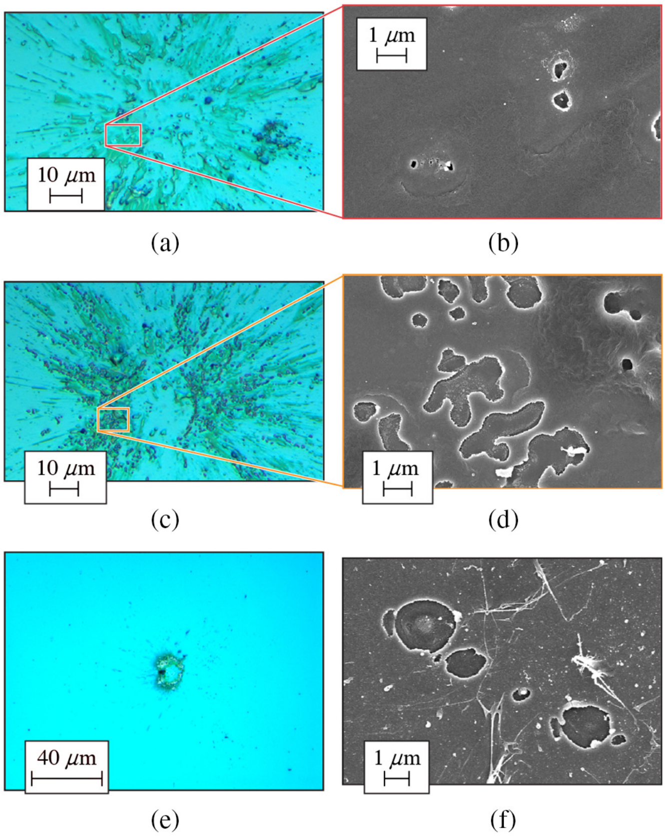

(a) (b)

(c) (d)

(e) (f)

Fig. 12 Site morphology of two-pulse exposures. Parameters: (a), (b) PE, 10 ps, 2.5 $\mathrm{J/cm^2}$, (c), (d) PE, 0.6 ps, 0.8 $\mathrm{J/cm^2}$, (e) glass, 10 ps, 1.9 $\mathrm{J/cm^2}$, (f) PTFE, 0.6 ps, 0.38 $\mathrm{J/cm^2}$. The laser was incident from right at a 45-deg angle of incidence.

0.6 ps, as shown in Figs. 11(c) and 11(d). The first pulse damage of Fig. 11(c) [same site as Fig. 9(e)] had sufficiently high incident fluence (~68% of the pristine coating LIDT) to demonstrate that nominally transparent particles can still form a multibeam interference pattern of damage in addition to the crater from microlensing. The second pulse interaction again shows widening of existing damage as well as generation of new ripples. This damage growth was especially prominent at 0.6 ps, consistent with damage driven primarily by electric field intensity.

As discussed earlier, the secondary contamination from glass microspheres involves generation of fragmentation debris [see Fig. 9(b), 0.55 $\mathrm{J/cm^2}$]. With sufficient fluence, subsequent exposure to a 10-ps pulse is observed to remove most of these fragments, although a small feature (ablation or scald) is formed at the previous location of glass fragments. Figure 12(e) shows a two-pulse glass site at 1.9 $\mathrm{J/cm^2}$. Besides the one-pulse features (microlensing crater and plasma scald that have completely etched the outer coating layer), the surrounding region is decorated by many dark submicron features, many of which correspond to nanoscalds/craters. Although these two images are from different interaction sites, the data set of two-pulse sites contained significantly less microparticle fragments than one-pulse sites. This suggests that the submicron features are created on the optic via microlensing by the fragments, concurrent with removal of the fragments.

The two-pulse results for PE microspheres show partial removal of the secondary contamination produced by the first pulse, accompanied by damage initiation at each of those removal locations. This occurred for both 10- and 0.6-ps pulses, as shown in Figs. 12(a)–12(d). For 10-ps pulses [Figs. 12(a) and 12(b)], craters and scalds are formed with nanoscale lateral dimension, surrounded by a region that is absent of secondary contamination. This suggests that the contours of the splash pattern of secondary contamination that was formed by the first pulse cause local microlensing during exposure to the second pulse, generating the small damage craters on the optic. The removal of the surrounding material is likely mainly due to the pressure from the underlying ablation crater. The results for 0.6-ps pulses [Figs. 12(c) and 12(d)] show similar morphologies, with damage craters surrounded by a region of contamination removal. Comparing the two pulse durations, the 0.6-ps morphologies show an increased area of damage for a given area of contamination removal.

Examination of the two-pulse sites for PTFE microparticles did not allow the drawing of conclusive understanding of the processes involved due to their irregular shapes. Nonetheless, damage growth could be observed, especially with 0.6-ps pulses. An example of this growth is shown in Fig. 12(f), seen as a single ripple on the left side of several of the craters.

Further work would be necessary to gain a more thorough and quantitative understanding of these multipulse interactions with short pulses, but these preliminary results show that the initial damage and secondary contamination continues to evolve, often unfavorably, with subsequent pulses. Furthermore, the preliminary damage growth thresholds in this work appear to be in the range 30% to 60% of the pristine LIDT, which is consistent to the growth threshold reported in literature: ∼50% of the pristine LIDT for multilayer dielectric mirrors.[34]

3.6 *Prediction for Other Particle Shapes and Sizes*

The use in this work of nominally spherical particles (both reflective and refractive) serves as a good starting point for the quantitative determination of damage behavior of a realistic optical component where micron-sized contamination particles or debris (of various shapes, stoichiometry and size) are present.

A sphere, because of its perfect symmetry, represents the maximum practical field enhancement scenario. In reality, contamination microparticles are expected to have arbitrary shapes and would be likely to have a much lower field enhancement factor. However, we can demonstrate that there is also a minimum field enhancement factor that cannot be avoided.

For instance, a small section of a glass surface will have a reflected amplitude of about 0.2, which will result in a two-beam interference pattern on the surface with maximum intensity of about 1.4. A metal surface will have a maximum intensity of about 4 due to (a minimum) two-beam interference.

In subsequent studies, we will extend this work both theoretically and experimentally to provide a better understanding about distribution of the field enhancement factor for realistic debris particles on optical surfaces, including subwavelength particles.

All of the above discussion has been limited to particles of approximate size larger than the scale of the laser wavelength. We expect that as particle size decreases and approaches this regime, the distribution of laser intensity will transition from a geometric-optical description to a distribution governed by diffraction. In this regime, the amplitude of laser intensification is less sensitive to the shape of the particle, and is instead more sensitive to its optical thickness (volume). However, since the decreasing size of the particle causes much of the particle to be in closer proximity to the optical surface, consideration of additional resonances of the particle may become necessary. For metallic particles, surface plasmon resonances (SPR) may lead to increased localized absorption, but would also create regions of electric field intensification near the particle which are strongly dependent on shape and orientation relative to laser polarization. For transparent particles, additional intensification may occur by excitation of whispering-gallery modes (WGM), which would have the largest potential effect for smooth symmetric particles such as nanospheres. Redeposited nanoparticulate ejecta from laser-induced damage events may be relevant candidates for such resonances, since molten droplets can form high-quality spheroid particles due to surface tension before cooling. Accurate theoretical treatment of intensification by nanoparticles should include all of these considerations.

4 Discussion

For the application of large-aperture laser systems, damage performance of optics includes not only control of initial damage initiation but also the ability to maintain that performance over the desired operational lifetime. Two aspects of primary concern are the generation of new damage sites and the growth of existing sites. The above results deal with the potential effects of particle contamination with short pulses and therefore have several implications with respect to these concerns.

First, the presence of contamination microparticles on the surface should be expected to cause the initiation of damage at fluences far lower than would be expected for the pristine optic. Even the generation of a small ablation crater introduces a vulnerability to damage growth, which can grow linearly in the damaged area[34] with each subsequent pulse. Eventually, it will reach a size that is no longer tolerable in the given application. Furthermore, the secondary contamination caused by optically transparent particles was observed in this work to also have the potential to generate new damage sites, further increasing the area susceptible to damage growth.

Another major concern is the potential for new damage initiation on downstream optics due to a significant area of damage and/or contamination, which causes beam modulation and intensification after some propagation distance. PE secondary contamination was found to be particularly apt to disperse over a large area, implying that it may be of particular concern for generating phase objects (modulating the beam phase). Future experiments plan to characterize the beam modulations induced by these PE contamination sites. Since the low melting point of PE was identified as the likely cause of the prevalent liquid splashing, other low-melting-point materials would similarly be expected to be problematic toward this end.

Steel microspheres did not exhibit splashing of microscale liquid droplets with picosecond pulses used in this work, but they were observed to disperse a layer of nanoparticles across a radius on the order of 100 μm or larger, depending on fluence. Although these could be partially removed by subsequent pulses, the coating was observed to be scalded by that removal process. Therefore, a large area of nanoparticle secondary contamination could become a relevant amplitude (or phase) object, possibly as a metallic or scalded region in addition to locally compromising the optical quality of the coating.

5 Conclusions

We have performed experiments to study the optical damage and secondary contamination caused by the interaction of 0.6- and 10-ps laser pulses with 40-μm microparticles on a multilayer dielectric mirror. The particles were observed to significantly reduce the LIDT, compared with its pristine coating value, due to localized intensification of the laser by the interaction with the particle. This intensification was determined to result from one of two mechanisms: (1) multibeam interference effects for reflective particles or (2) microlensing by transparent model-contaminant particles. In addition to ablation craters formed on the optical coating due to these mechanisms, ablation events were observed to initiate on the particles as well. The ablation from the particle was responsible for the generation of secondary contamination in the form of nanoparticles, fragments, and liquefied jets. Furthermore, the ablation plume expanding from the particle was observed to locally cause plasma scalding of the optic for 10-ps pulses. A second pulse incident on the resulting sites caused damage growth, as well as the initiation of new damage sites from portions of the secondary contamination. All of these show that the contamination microparticles can be a potent precursor for optical damage, causing initiation far below the pristine LIDT, and thereby exposing optics to the potential for damage growth. The evidence provided by this work demonstrates the importance to further investigate cleanliness protocols and damage growth for the applications of large-aperture, short-pulse laser systems.

Acknowledgments

This material was based upon work supported by the Department of Energy National Nuclear Security Administration under Award Number DE-NA0003856, the University of Rochester, and the New York State Energy Research and Development Authority. This report was prepared as an account of work sponsored by an agency of the U.S. Government. Neither the U.S. Government nor any agency thereof, nor any of their employees, makes any warranty, express or implied, or assumes any legal liability or responsibility for the accuracy, completeness, or usefulness of any information, apparatus, product, or process disclosed, or represents that its

use would not infringe privately owned rights. Reference herein to any specific commercial product, process, or service by trade name, trademark, manufacturer, or otherwise does not necessarily constitute or imply its endorsement, recommendation, or favoring by the U.S. Government or any agency thereof. The views and opinions of authors expressed herein do not necessarily state or reflect those of the U.S. Government or any agency thereof. The authors have no relevant financial interests in the manuscript and no other potential conflicts of interest to disclose.

References

1. J. D. Lindl et al., "The physics basis for ignition using indirect-drive targets on the National Ignition Facility," *Phys. Plasmas* **11**(2), 339–491 (2004).
2. N. Fleurot, C. Cavailler, and J. L. Bourgade, "The laser Mégajoule (LMJ) project dedicated to inertial confinement fusion: development and construction status," *Fusion Eng. Des.* **74**(1–4), 147–154 (2005).
3. S. Jiang et al., "Experimental progress of inertial confinement fusion based on ShenGuang III laser facility in China," *Nucl. Fusion* **59**(3), 032006 (2019).
4. J. M. Soures et al., "Direct-drive laser-fusion experiments with the OMEGA, 60-beam, >40-kJ, ultraviolet laser system," *Phys. Plasmas* **3**(5), 2108–2112 (1996).
5. S. Gales et al., "The extreme light infrastructure—nuclear physics (ELI-NP) facility: new horizons in physics with 10 PW ultra-intense lasers and 20 MeV brilliant gamma beams," *Rep. Prog. Phys.* **81**(9), 094301 (2018).
6. Z. Zhang et al., "The 1 PW/0.1 Hz laser beamline in SULF facility," *High Power Laser Sci. Eng.* **8**, e4 (2020).
7. J. H. Sung et al., "4.2 PW, 20 fs Ti:Sapphire laser at 0.1 Hz," *Opt. Lett.* **42**(11), 2058–2061 (2017).
8. A. Casner et al., "LMJ/petal laser facility: overview and opportunities for laboratory astrophysics," *High Energy Density Phys.* **17**(Part A), 2–11 (2015).
9. J. Myatt et al., "High-Intensity laser interactions with mass-limited solid targets and implications for fast-ignition experiments on OMEGA EP," *Phys. Plasmas* **14**(5), 056301 (2007).
10. M. L. Spaeth et al., "Description of the NIF laser," *Fusion Sci. Technol.* **69**(1), 25–145 (2016).
11. H. Shiraga et al., "Fast ignition integrated experiments with Gekko and LFEX lasers," *Plasma Phys. Control. Fusion* **53**(12), 124029 (2011).
12. C. J. Stolz et al., "Transport mirror laser damage mitigation technologies on the National Ignition Facility," *Proc. SPIE* **10691**, 106910W (2018).
13. M. J. Matthews et al., "Phase modulation and morphological evolution associated with surface-bound particle ablation," *J. Opt. Soc. Am. B* **30**(12), 3233–3242 (2013).
14. R. N. Raman et al., "Damage on fused silica optics caused by laser ablation of surface-bound microparticles," *Opt. Express* **24**(3), 2634–2647 (2016).
15. S. G. Demos et al., "Mechanisms governing the interaction of metallic particles with nanosecond laser pulses," *Opt. Express* **24**(7), 7792–7815 (2016).
16. S. R. Qiu et al., "Impact of laser-contaminant interaction on the performance of the protective capping layer of 1ω high-reflection mirror coatings," *Appl. Opt.* **54**(29), 8607–8616 (2015).
17. S. G. Demos et al., "Dynamics of secondary contamination from the interaction of high-power laser pulses with metal particles attached on the input surface of optical components," *Opt. Express* **27**(16), 23,515–23,528 (2019).
18. S. G. Demos and R. A. Negres, "Morphology of ejected particles and impact sites on intercepting substrates following exit-surface laser damage with nanosecond pulses in silica," *Opt. Eng.* **56**(1), 011016 (2017).
19. C. W. Carr et al., "Damage sources for the NIF grating debris shield (GDS) and methods for their mitigation," *Proc. SPIE* **10447**, 1044702 (2017).
20. T. Jitsuno et al., "Recent progresses on insights of laser damage mechanisms and influence of contamination in optics," *Proc. SPIE* **8786**, 87860B (2013).

21. A. A. Kozlov et al., "Long-term monitoring the damage performance of multilayer dielectric grating samples residing inside the compressor chamber of the OMEGA EP laser," *Opt. Eng.* **60**(3), 031008 (2020).
22. K. R. P. Kafka and S. G. Demos, "Interaction of short laser pulses with model contamination microparticles on a high reflector," *Opt. Lett.* **44**(7), 1844–1847 (2019).
23. S. G. Demos, C. W. Carr, and D. A. Cross, "Mechanisms of surface contamination in fused silica by means of laser-induced electrostatic effects," *Opt. Lett.* **42**(13), 2643–2646 (2017).
24. A. A. Kozlov et al., "Mechanisms of picosecond laser-induced damage in common multilayer dielectric coatings," *Sci. Rep.* **9**, 607 (2019).
25. J. Perrière et al., "Nanoparticle formation by femtosecond laser ablation," *J. Phys. D Appl. Phys.* **40**(22), 7069–7076 (2007).
26. B. R. Tull et al., "Formation of silicon nanoparticles and web-like aggregates by femtosecond laser ablation in a background gas," *Appl. Phys. A* **83**(3), 341–346 (2006).
27. B. Tan and K. Venkatakrishnan, "Synthesis of fibrous nanoparticle aggregates by femtosecond laser ablation in air," *Opt. Express* **17**(2), 1064–1069 (2009).
28. P. Miglietta et al., "Mg-based photocathodes prepared by ns, ps and fs PLD for the production of high brightness electron beams," *Appl. Surf. Sci.* **255**(10), 5228–5231 (2009).
29. H. Wang et al., "Origin of the plasma scalds in dielectric coatings induced by 1ω laser," *Appl. Phys. Lett.* **108**(14), 141603 (2016).
30. X. Ling, S. Liu, and X. Liu, "Defect induced thermal-plasma coupling damage in optical films under nanosecond pulse laser irradiation," *Phys. Scr.* **94**(12), 125707 (2019).
31. F. Genin and C. Stolz, "Morphologies of laser-induced damage in hafnia-silica multilayer mirror and polarizer coatings," *Proc. SPIE* **2870**, 439–448 (1996).
32. M. Chambonneau et al., "Origin of the damage ring pattern in fused silica induced by multiple longitudinal modes laser pulses," *Appl. Phys. Lett.* **104**(2), 021121 (2014).
33. M. Sozet et al., "Sub-Picosecond laser damage growth on high reflective coatings for high power applications," *Opt. Express* **25**(21), 25767–25781 (2017).
34. M. Sozet et al., "Laser damage growth with picosecond pulses," *Opt. Lett.* **41**(10), 2342–2345 (2016).

Kyle R. P. Kafka received his PhD in physics from Ohio State University. Currently, he is a scientist at the Laboratory for Laser Energetics, University of Rochester, where his research interests include laser damage and material dynamics.

Brittany N. Hoffman received her BS degree in engineering physics from Ohio State University in 2010 and her MS degree in optics from the University of Rochester in 2016. She joined the Laboratory for Laser Energetics in 2010. Currently, she is a research engineer at the Laser Lab, where her research interests center around diffraction gratings and laser damage testing.

Hu Huang received his PhD from the University of Rochester. Currently, he is a staff scientist at the Laboratory for Laser Energetics, University of Rochester.

Stavros G. Demos received his PhD in physics from City University of New York. He is a distinguished scientist at the Laboratory for Laser Energetics, University of Rochester.